A New and Facile Method To Prepare Uniform Hollow MnO/Functionalized $mSiO_2$ Core/Shell Nanocomposites

Yung-Kang Peng,[†] Chih-Wei Lai,[†] Chien-Liang Liu,[†] Hsieh-Chih Chen,[†] Yi-Hsuan Hsiao,[†] Wei-Liang Liu,[‡] Kuo-Chun Tang,[†] Yun Chi,[‡] Jong-Kai Hsiao,[§,⊥,*] Kun-Eng Lim,[§,⊥] Hung-En Liao,[§] Jing-Jong Shyue,[∥] and Pi-Tai Chou[†,*]

[†]Department of Chemistry, National Taiwan University, Taipei 106, Taiwan, [‡]Department of Chemistry, National Tsing Hua University, Hsinchu 300, Taiwan, [§]Department of Medical Imaging, Buddhist Tzu Chi General Hospital, Taipei Branch, Taiwan, [⊥]School of Medicine, Tzu Chi University, Hualien, Taiwan, and [∥]Research Center for Applied Science, Academia Sinica, Taipei 115, Taiwan

ABSTRACT Trifunctional uniform nanoparticles comprising a manganese nanocrystal core and a functionalized mesoporous silica shell (MnO@$mSiO_2$(Ir)@PEG, where Ir is an emissive iridium complex and PEG is polyethylene glycol) have been strategically designed and synthesized. The T_1 signal can be optimized by forming hollow core (H-MnO@$mSiO_2$(Ir)@PEG) *via* a novel and facile etching process, for which the mechanism has been discussed in detail. Systematic investigation on correlation for longitudinal relaxation (T_1) *versus* core shapes and shell silica porosity of the nanocomposites (MnO, H-MnO, MnO@SiO_2, MnO@$mSiO_2$, H-MnO@$mSiO_2$) has been carried out. The results show that the worm-like nanochannels in the mesoporous silica shell not only increase water permeability to the interior hollow manganese oxide core for T_1 signal but also enhance photodynamic therapy (PDT) efficacy by enabling the free diffusion of oxygen. Notably, the H-MnO@$mSiO_2$(Ir)@PEG nanocomposite with promising r_1 relaxivity demonstrates its versatility, in which the magnetic core provides the capability for magnetic resonance imaging, while the simultaneous red phosphorescence and singlet oxygen generation from the Ir complex are capable of providing optical imaging and inducing apoptosis, respectively.

KEYWORDS: T_1 contrast agent · MnO · hollow MnO · mesoporous silica · dual imaging · photodynamic therapy

Magnetic resonance imaging (MRI) has received much attention over the past two decades as a technique for the clinical diagnosis owing to a number of advantages such as unlimited tissue penetration, zero ionizing radiation, and its noninvasive nature, *etc.*[1−3] Magnetic nanocolloids possess higher water proton relaxivities than molecular chelates because metal ions in nanoparticles are densely populated. Contrast agents, such as superparamagnetic iron oxides (SPIOs) and ultrasmall SPIOs with high T_2 relaxivities, are widely used in tumor targeting and imaging.[4−8] Since T_2-weighted imaging usually produces confusion with the signals from bleeding, its T_1-weighted counterpart (positive contrast), which is subject to less artifacts and higher signal intensity of the target organs and tissues, provides advantageous alternatives. In light of this development, the manganese oxide nanoparticles (MnO NPs) have recently proven to be interesting candidates as contrast agents by shortening the longitudinal (or spin−lattice) relaxation time T_1.[9]

However, a major requirement for a successful application of magnetic NPs in biomedicine, in particular, for *in vivo* imaging, is to possess good colloidal stability and low toxicity in a biological environment. To endow these hydrophobic MnO NPs with hydrophilic and biocompatible properties, various surface modification methods are adopted. The PEG (polyethylene glycol)-phospholipid block copolymers could form a micelle structure *via* the hydrophobic interaction between hydrophobic tail groups of surfactants and phospholipid parts.[10] Besides, specific targeting is another consideration for MnO NPs, which can be prepared by conjugating PEG-phospholipid with Her-2/neu receptor antibody.[9] Schladt *et al.* fabricated multifunctional MnO NPs functionalized with a dopamine-PEG-protoporphyrin IX (DA-PEG-PP) ligand for simultaneous optical and MRI imaging and cancer treatment using photodynamic therapy (PDT).[11]

The above-mentioned approaches require sophisticated and elaborate ligand design to anchor MnO NPs for specific targeting, optical imaging, biocompatible and drug delivery properties. Syntheses of these multifunctionalized ligands, however, are nontrivial, cost demanding, and may not be applicable for large-scale production. Another strategy for surface modification is the formation of biocompatible shells around the NPs. As for shell coating, silica

* Address correspondence to jongkai@tzuchi.com.tw, chop@ntu.edu.tw.

Received for review March 10, 2011 and accepted April 25, 2011.

Published online May 06, 2011
10.1021/nn200928r

has been widely applied to protect the NPs from the external environment and thereby improve the stability and biocompatibility of the NPs.[12] It is also relatively much easier to incorporate dyes and photosensitizers into the silica framework and modify amines, carboxyl groups, antibodies, and PEG, *etc*., onto the silica outermost surface by end-labeled silane derivatives *via* the facile sol−gel chemistry. Unfortunately, with the nonporous silica shell coating, the manganese oxide core might not be easily accessible with water molecules. This is mainly due to the fact that nonporous silica slows down the exchange rate of water molecules.[9,13]

Recently, hollow MnO NPs became a focusing issue. Hyeon and co-workers have synthesized hollow MnO nanoparticles with acid etching under high temperature (300 °C) using the impurity alkylphosphonic acid in technical grade of TOPO as the etchant attributed to Kirkendall effect.[14] This effect comes from the outward diffusion of the constituting materials, and the simultaneous inward diffusion of vacancies results in the formation of a void in the core. The hollow Mn_3O_4 nanoparticles were then synthesized by oxidation of the surface of MnO nanoparticles under prolonged reaction time (this takes several days), followed by selective removal of the core of nanoparticles in an acidic buffer.[10] Notably, hollow structured MnO NPs showed superior spin relaxation enhancement effect due to the increased concentration of MR-active Mn^{2+} ions exposed at the hollow inner surface for contacting with water.[10,14] Moreover, hollow MnO nanoparticles have been reported to enhance the spin relaxation up to 6-fold and possess a unique property of a nanocavity suited for potential drug delivery *in vivo*.[10]

Herein, we employ a new and facile method to prepare hollow manganese oxide nanoparticles using simple chemicals, ethylacetate and sodium hydroxide, under relatively much lower temperature (60 °C) and shorter reaction time (<10 h). In this synthetic protocol, the carboxylate anion potentially acts as a ligand to extrude the core MnO *via* Kirkendall effect (*vide infra*), forming hollow MnO (H-MnO) nanoparticles. This etching process is very mild, as demonstrated by co-condensation of an Ir(III) complex phosphorescence dye into H-MnO(core)/SiO_2(shell), which retains its intense phosphorescence after etching, forming H-MnO/SiO_2(Ir) core/shell nanoparticles (Ir: an Ir(III) complex). We then moved one more step to prepare a novel core−shell nanostructure (H-MnO@mSiO_2), in which the hollow core is buried in the mesoporous silica (mSiO_2) shell. Despite the well-established synthetic protocols on nanostructural magnetic nanoparticle core and silica shell,[15−20] to the best of our knowledge, there have been no reports on encapsulation of hollow Mn(+2)O nanoparticles with mesoporous silica shell and its bioapplication.

Also, in this study, a series of nanostructures, including MnO, H-MnO, MnO@SiO_2, MnO@mSiO_2, and H-MnO@mSiO_2, were prepared, in which the core MnO could be in a solid sphere or hollow shape, while shell SiO_2 could be nonporous or mesoporous, so that systematic investigation of correlation on longitudinal relaxation (T_1) *versus* core shapes and shell silica porosity of the nanocomposites can be carried out. Finally, the H-MnO@mSiO_2(Ir)@PEG nanocomposite with promising r_1 relaxivity is then used to demonstrate its versatility in magnetic resonance imaging, phosphorescence imaging, and singlet oxygen production, that is, the potential in photodynamic therapy (PDT). Details are elaborated upon in the following sections.

RESULTS AND DISCUSSION

Synthesis and Characterization. Using the final-stage nanocomposite H-MnO@mSiO_2(Ir)@PEG as the prototype, Scheme 1 illustrates the overall synthetic protocol. First of all, manganese oxide nanocrystals are synthesized by using a facile thermal decomposition method.[21] These nanocrystals are typically stabilized by hydrophobic oleic acid ligands and then transferred to the aqueous phase by utilizing cetyltrimethylammonium bromide (CTAB). In the subsequent sol−gel reaction, CTAB-stabilized nanocrystals act as seeds for the formation of spherical mesoporous silica shells by hydrolysis and condensation of tetraethylorthosilicate (TEOS). Herein, CTAB serves as not only the stabilizing secondary surfactant for the transfer of the nanocrystals to the aqueous phase but also the organic templates for the formation of the mesoporous silica shells. The structure of the as-synthesized iridium complex ([5-pyridyl-3-(butyl triethoxysilyl)pyrazolate]$_1$[phenyl isoquinolinate]$_2$ iridium) (Ir(III) complex) (Figure 1A) is advanced by intentionally direct connecting the $(EtO)_3Si$ functional group, so that it is simultaneously encapsulated into the mesoporous silica framework during the co-condensation reaction. This new strategic design can avoid any possible leakage of the iridium complex, such as [Ir(piq)$_2$(ppTES)] (see Figure 1B), used in our previous report,[22] due to the relative weak ligation between the sensitizer part and the silanol group.

In this core/shell structure, the silica−CTAB layer is formed around the CTAB−MnO nanoparticles under basic conditions through an electrostatic interaction between the cationic (CTAB) and anionic (silicate) species.[23] To further fabricate hollow MnO within a core−shell nanocomposite, EA/NaOH(aq) (3 mL of EA and 50 mL of H_2O (4 mg of NaOH)) solution is then introduced. The hollow MnO core of H-MnO@mSiO_2(Ir) could be obtained by applying the etching process to the as-synthesized nanocomposite, MnO@mSiO_2(Ir). Details of the associated mechanism will be discussed in the following section. H-MnO@mSiO_2(Ir) was then

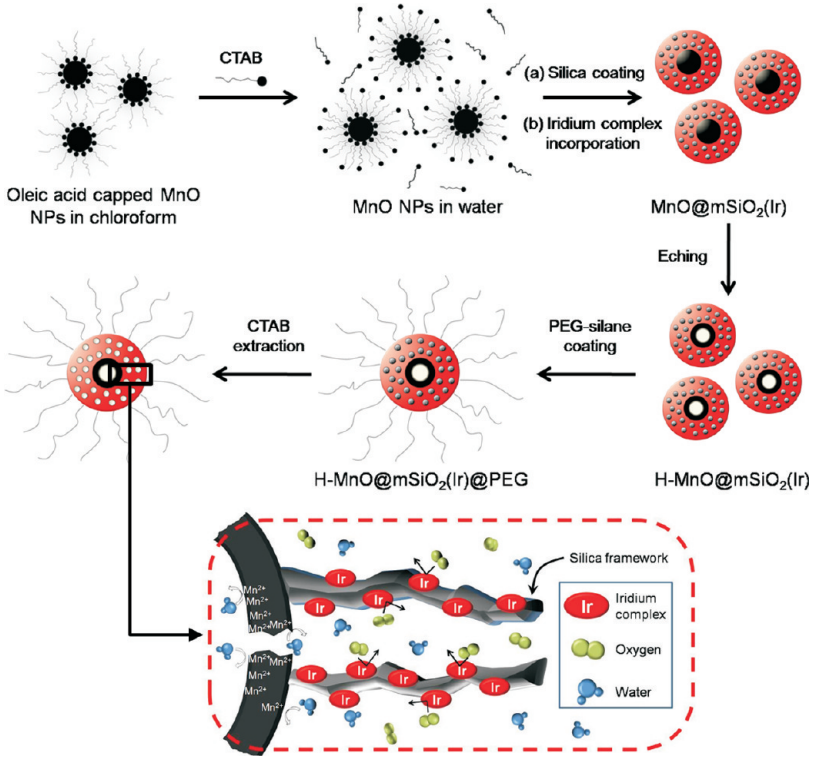

Scheme 1. Schematic illustration of the synthetic procedure for H-MnO@mSiO$_2$(Ir)@PEG nanocomposites.

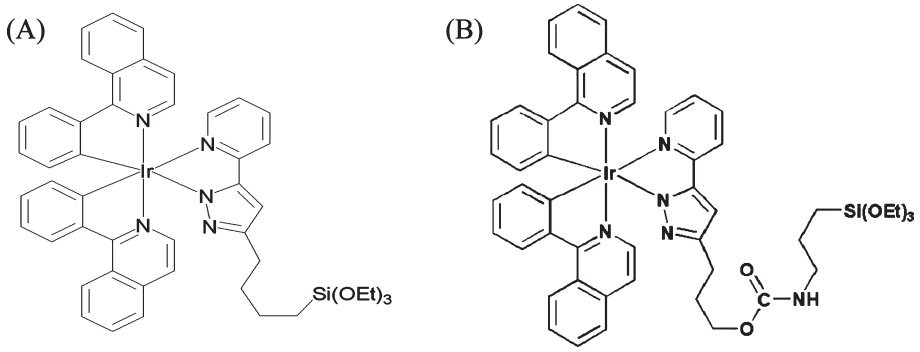

Figure 1. (A) Ir(III) complex used in this study, compared with (B) [Ir(piq)$_2$(ppTES)] used in ref 25.

modified by silane-functionalized PEG on the outmost surfaces. The CTAB templates were then removed *via* an ion exchange method,[24] leaving the void of nanochannels, which not only enhances PDT efficiency by enabling the free diffusion of oxygen but also increases water permeability to the interior hollow manganese oxide core for T_1 signal. Note that the reverse process, that is, removing CTAB, followed by modification with PEG, causes the obstruction of the nanochannels due to the penetration of PEG (*vide infra*).

Physical and Photophysical Properties. Figure 2A shows the transmission electron microscopy (TEM) image of the oleic-acid-capped MnO nanocrystals, which are synthesized by thermal decomposition of Mn-oleate in octadecene. As depicted, the as-prepared oleic-acid-capped MnO NPs are homogeneous and well-dispersed. The average diameter is about 23.4 $\pm$ 0.7 nm according to the TEM image. Prior to coating the mesoporous silica shell onto the MnO nanoparticles, the oleic-acid-capped MnO NPs have been surface modified by CTAB, the resulting size of which remained unchanged in aqueous solution (Figure S1A in Supporting Information). After coating the silica shell, modifying PEG on outmost surface, followed by CTAB extraction *via* ion exchange, Figure 2B shows the image of the MnO@mSiO$_2$(Ir)@PEG nanocomposite, in which the mesoporous silica shell clearly possesses a worm-like channel. The average size of the as-prepared nanocomposites is measured to be 80 $\pm$ 2.5 nm in diameter. After treatment of MnO@mSiO$_2$(Ir)@PEG with EA/NaOH, the TEM image of the resulting H-MnO@mSiO$_2$(Ir)@PEG nanocomposite (Figure 2C) reveals negligible changes in diameter for both MnO and SiO$_2$, in which each H-MnO core is encapsulated by a

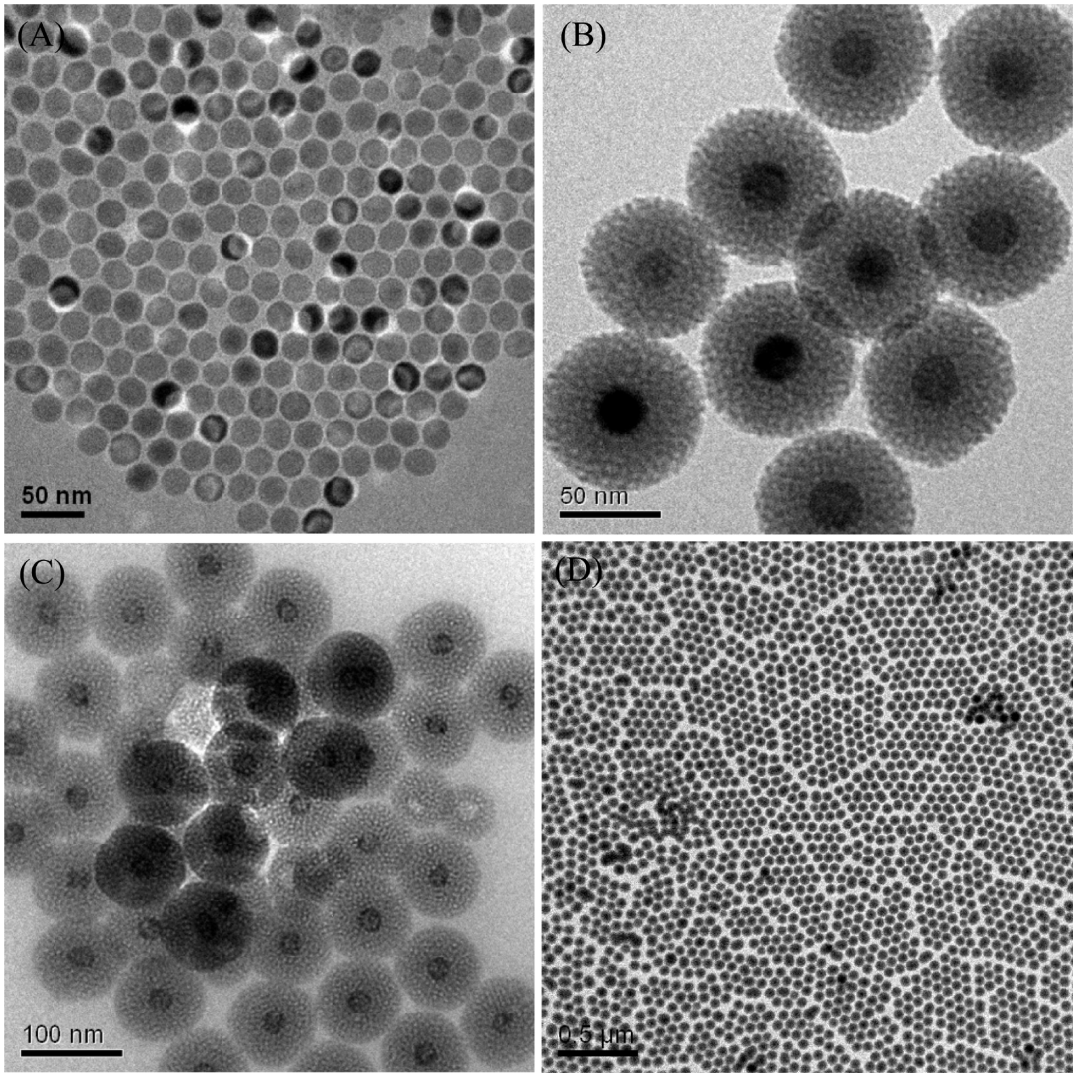

Figure 2. TEM of (A) oleic-acid-capped MnO nanocrystals, (B) MnO@mSiO$_2$(Ir)@PEG, (C,D) high- and low-magnification images of H-MnO@mSiO$_2$(Ir)@PEG nanoparticles, respectively.

~30 nm thick silica layer. The size of H-MnO@mSiO$_2$-(Ir)@PEG is very uniform, as evidenced by the uniformity (σ< 3.5%) (statistic in Figure S1B in Supporting Information) of the as-prepared nanocomposites covering a large area (3.5 × 3.5 μm^2) in the TEM image (Figure 2D). The diameter could be easily controlled by varying the concentration of the core nanocrystals during the formation of the mesoporous silica shell (Figure S2). The N_2 adsorption–desorption isotherms (see Figure S3) exhibit a characteristic type *IV* isotherm according to the IUPAC classification,[25] demonstrating their mesoporous characteristics. The average pore diameter calculated using the Barrett–Joiner–Halenda (BJH) method was 2.2 nm, and the Brunauer–Emmett–Teller (BET) surface area is measured to be 660 m^2 g^{-1}.

Figure 3 reveals the X-ray powder diffraction (XRD) patterns of the as-prepared MnO nanoparticles, MnO@mSiO$_2$(Ir)@PEG and H-MnO@mSiO$_2$(Ir)@PEG nanocomposites. In the beginning, the amorphous silica structure peak at 2θ = 23° of the inert surface of

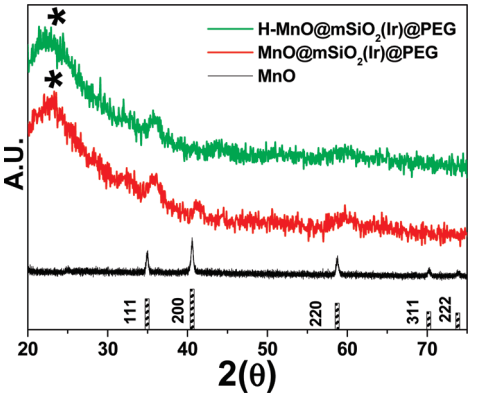

Figure 3. X-ray diffraction spectra of MnO, MnO@mSiO$_2$-(Ir)@PEG, and H-MnO@mSiO$_2$(Ir)@PEG nanoparticles.

MnO@mSiO$_2$(Ir)@PEG and H-MnO@mSiO$_2$(Ir)@PEG is observed. As for the MnO nanoparticles, the cubic structure with characteristic peaks of (111), (200), (220), (311), and (311) are well-resolved from the X-ray

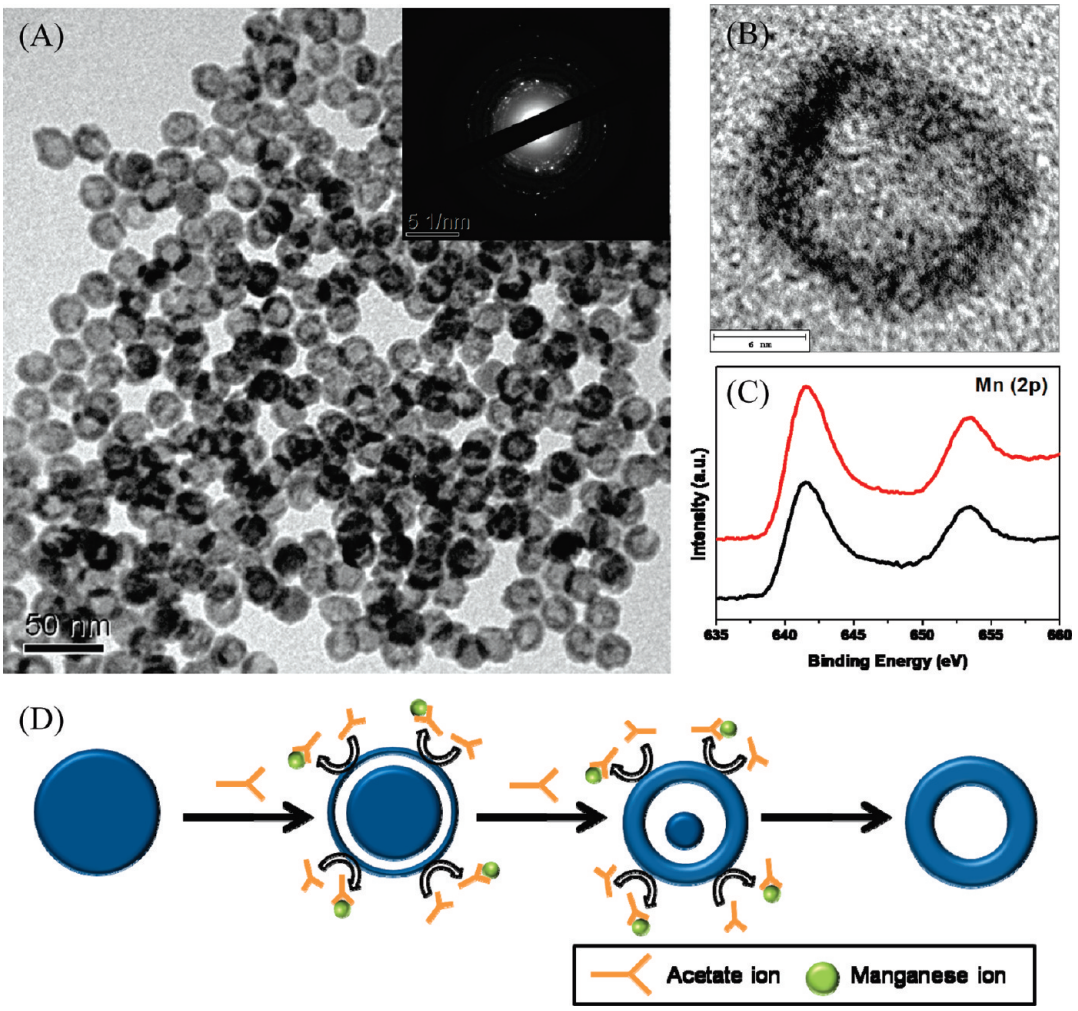

Figure 4. (A) TEM image of hollow manganese oxide (H-MnO) nanoparticles. Inset: SAED pattern. (B) High-resolution TEM image of H-MnO NPs (scale bar: 6 nm). (C) XPS spectra for MnO nanocrystals before (blue) and after (red) the etching process. (D) Schematic for the evolution of the morphologies of the particles.

diffraction (XRD) pattern of MnO@mSiO_2(Ir)@PEG and H-MnO@mSiO_2(Ir)@PEG.

The hollow MnO NPs are further characterized by high-resolution TEM (HR-TEM), electron diffraction (ED), and X-ray photoelectron spectroscopy (XPS). The HR-TEM images (Figure 4B) and ED pattern (see inset of Figure 4A) indicate that the hollow MnO nanoparticles have a lattice spacing of 2.2 Å and still remain a highly crystalline structure (cubic) similar to that of the original MnO NCs. The XPS (Figure 4C) provides the information on the oxidation state of manganese cations, the results of which indicate that there is no significant change in the oxidation state (+2) before and after EA/NaOH(aq) solution treatment. With all data provided (including the XRD spectra), the etching process developed in this study causes no changes in either oxidation states or crystallinity. The results are in stark contrast to previously reported methods, claiming the change of either oxidation state (+2 to +3)[10] or crystallinity (cubic to amorphous)[14] upon forming a hollow structure from solid manganese oxide nanoparticles. The difference lies in the fact that the protocol developed in this study exploits low reaction temperature (~60 °C) and short reaction time (<10 h), such that no redox reaction[10] and no alternation of crystallinity[14] take place.

The finding that EA/NaOH(aq) solution is able to facilitate the transformation of MnO NCs to a hollow structure is of fundamental interest and is worthy of further in-depth investigation. Thus, the associated mechanism is pursued by conducting a variety of controlled experiments to etch the bare MnO NCs. First of all, when only NaOH(aq) is added to execute the etching process, no hollow-shaped nanoparticles are produced. As for the second control experiment, only EA-H_2O cosolvent is applied without addition of NaOH. To our surprise, the Kirkendall effect seems to be operative and the TEM image of the collected intermediates (see Figure S4A in Supporting Information) shows irregular morphology. We thus suspect that a small proton of EA may dissociate, generating the acetate anions that is able to chelate the metal ion,

which then gradually etches MnO from the inner core *via* Kirkendall effect. This process should be accelerated under base (*e.g.*, NaOH) catalysis. To test this hypothesis, we then monitor the etching of MnO NCs by using sodium acetate (CH_3COONa, 2 mM). Similarly, the results reveal the formation of hollow MnO NPs (mixed with yolk−shell intermediates) after 24 h reaction times (see Figure S4B). Moreover, during the early reaction period of ~10 h, the core−shell−void intermediate is also traceable, as shown by TEM images displayed in Figure S4C. Evidently, the sodium acetate also helps formation of hollow MnO NPs, supporting the proposed chelating mechanism. In comparison to the etching process using EA/NaOH(aq) solution, however, the use of sodium acetate gives inferior quality of the hollow MnO NPs in terms of homogeneity and particle dispersion (*c.f.*, Figure 4A and Figure S4B in Supporting Information). The evolution of the morphologies upon etching the particles is schematically depicted in Figure 4D. Four distinct stages amid the reaction can be categorized: the original solid MnO NC, the core−shell−void intermediate, the yolk−shell intermediate, and the final hollow structure. The EA/NaOH(aq) solution serves as a decent reagent, which undergoes gradual release of acetate anions to smoothly etch the inner core of MnO *via* the Kirkendall effect.

In an aim to achieve the multifunctionality of the nanocomposite, we then move one further step by incorporating the emissive dye during the sol−gel process. In this approach, an $(EtO)_3Si$-functionalized iridium complex (Ir(III) complex; see Figure 1A) is simultaneously encapsulated into the mesoporous silica framework by covalent bonding (see Methods for details), forming H-MnO@mSiO_2(Ir)@PEG. Figure S5 of the Supporting Information shows the red phosphorescence (λ_{max} = 600 nm) and corresponding excitation spectrum of the as-prepared H-MnO@mSiO_2(Ir)@PEG nanocomposites in both degassed and aerated solution. Note that the phosphorescence of the Ir(III) complex, due to the short radiative lifetime promoted by the heavy atom (Ir) spin−orbit coupling effect, is only quenched 70% from degassed ($\Phi_p \sim 0.9$, $\tau_p \sim 2.3$ μs) to aerated ($\Phi_p \sim 0.31$, $\tau_p \sim 0.80$ μs) aqueous solution.[22] The quenching of phosphorescence by O_2, generating singlet molecular oxygen, can be exploited in photodynamic therapy, while the remaining $\Phi_p \sim 0.31$ phosphorescence can thus be used for luminescence imaging.

In the above H-MnO@mSiO_2(Ir)@PEG nanocomposites, PEG is incorporated to avoid collapse of the pore and to increase the colloidal stability. Very recently, Lin *et al.* had reported that pore collapsing in PBS could be avoided by modification of PEG onto the mesoporous shell, which effectively masks the surface silanol group *via* the formation of a biocompatible layer.[26] To manifest the PEG modification in the current study,

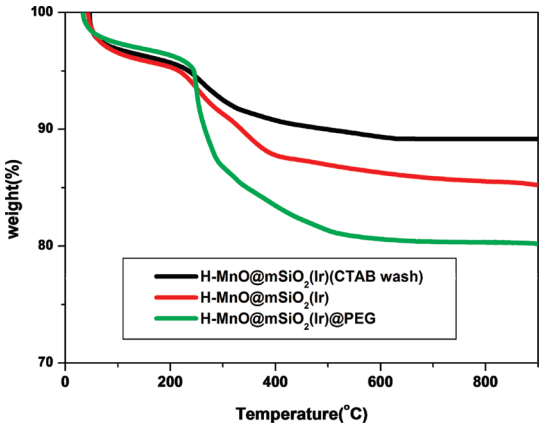

Figure 5. Thermal gravimetric analysis (TGA) of H-MnO@mSiO_2(Ir) (CTAB wash), H-MnO@mSiO_2(Ir), and H-MnO@mSiO_2(Ir)@PEG.

dynamic light scattering (DLS) has been performed and the results are shown in Figure S6 of the Supporting Information. DLS data of H-MnO@mSiO_2(Ir)@PEG reveal a mean hydrodynamic diameter about 98.4 nm in PBS solution. Compared to the particle sizes calculated from TEM images (see Figure 2C and statistics in Figure S1B), the larger size measured by DLS originates from the hydration layer of PEG coated onto the surface. Notably, template CTAB is hazardous and less biocompatible[27] and should be removed before any bioapplications. The removal of CTAB can be confirmed by zeta-potential measurement.[28] Without washing, the adsorption of the cationic surfactant leads to a positively charged surface of +50.5 mV. The gradual removal of the CTAB surfactant after two ion exchange procedures is reflected from the decrease of the zeta-potential measurements, stabilizing to a negatively charged −27.7 mV (see Figure S7). To further demonstrate the successful PEG modification and surfactant extraction, the results of TGA of H-MnO@mSiO_2 (see red line of Figure 5) reveal a ~10% weight loss of CTAB, oleic acid, and Ir(III) complex by heating above 250 °C. After extraction of CTAB, as clearly shown in Figure 5, much less weight loss of ~4% is obtained. The 6% difference in weight loss is then attributed to the removal of CTAB. After PEG modification, further weight loss (~14%, see green line in Figure 5) confirms that PEG is successfully functionalized on the silica surface.

Nowadays, many reports on manganese-related nanoparticles give various relaxivities, due to different field strength applied.[9−11,13,14,29−33] Here, in an aim to investigate longitudinal (T_1) relaxation time *versus* core shapes and shell silica porosity conditions of the nanocomposite, we then systematically measure the longitudinal relaxivity r_1 using a 0.47 T Minispec spectrometer (see Methods for details) as a function of the following nanoparticles: MnO, H-MnO, MnO@SiO_2 (Figure S8 in Supporting Information), MnO@mSiO_2, and H-MnO@mSiO_2 with controlled silica shell thickness

TABLE 1. Relaxation Properties of the Nanocomposites

material	r_1 (mM^{-1} s^{-1})	r_2 (mM^{-1} s^{-1})	r_2/r_1
MnO	0.17	5.18	30.47
H-MnO	0.92	7.48	8.13
MnO@SiO_2	0.07	1.54	22
MnO@mSiO_2	0.16	1.60	10
H-MnO@mSiO_2	0.2	1.78	8.9
H-MnO@mSiO_2(Ir)@PEG	0.2	1.76	8.8
	0.17 (3 T)	1.75 (3 T)	10.29
H-MnO@mSiO_2(Ir)@PEG*	0.14	1.69	12.07

around 30 nm. Based on the r_1 relaxivity value listed in Table 1, the hollow MnO nanoparticles (H-MnO) exhibit the highest r_1 value (0.92) among all titled NPs. H-MnO NPs possess both inner and outer surface (*c.f.* outer surface only for MnO NPs) to interact with water molecules, rationalizing the enhancement of r_1 relaxivity.[10,14] The trend of r_1 relaxivity is on the order of H-MnO@mSiO_2 (0.2) > MnO@mSiO_2 (0.16) > MnO@SiO_2 (0.07). Evidently, the r_1 relaxivity value decreases substantially from 0.17 in MnO NPs to 0.07 in MnO@SiO_2. Although water would be still permeable inside the amorphous silica shell to contact the Mn(II) ion on the surface of MnO NPs, the nonporous silica framework may diminish the r_1 relaxivity by shortening the exchange rate with water molecules. Surprisingly, both mesoporous silica modification species, MnO@mSiO_2 and H-MnO@mSiO_2, show the r_1 relaxivity value as high as that of bare MnO NCs. We attribute the high r_1 relaxivity to the existence of the worm-like nanochannels, such that the water exchanging rate can be facilitated. Due to additional inner Mn ion surface layers, the relatively higher relaxivity (0.2) could be attained in H-MnO@mSiO_2. Nevertheless, this value is still smaller than that of H-MnO (0.92) by more than 3-fold. It is believed that the hydroxyl group on the surface of MnO might partially participate in the sol–gel process, forming to a silica layer that blocks water molecules to reach the surface Mn ion. No significant decrease of r_1 relaxivity (0.2) was observed after incorporating an Ir(III) complex and modifying PEG onto the outmost surface (H-MnO@mSiO_2(Ir)@PEG). It should be noted that, if CTAB is extracted before PEG modification, forming H-MnO@mSiO_2(Ir)@PEG* as opposed to regular H-MnO@mSiO_2(Ir)@PEG synthesized here (*i.e.*, PEG modification, followed by CTAB extraction), the r_1 value apparently decreases to 0.14. Such a postgrafting PEG step makes silanols more easily functionalized on the inner nanochannel surface and thus hampered the diffusion of water from the surrounding environment to the core part. We have also carried out a systematic study in an aim to optimize the r_1 value using H-MnO@mSiO_2 and found that the thickness of both of the core hollow MnO and mesoporous shell were able to tune the r_1 value. On the one hand, the r_1 value decreases as the thickness of the mesoporous shell increases. On the other hand, the r_1 value seems to reach an optimum value upon forming hollow MnO with a shell thickness of 30 nm. Further etching gradually decreases the r_1 value. In theory, the r_1 value will finally close to that of pure water upon completely etching MnO, forming the hollow mesoporous silica. For the purpose of their cellular test (*vide infra*) and future clinically related application, the relaxivity of H-MnO@mSiO_2(Ir)@PEG was further measured at higher field (3 T), giving lower r_1 (0.17 mM^{-1} s^{-1}) and similar r_2 values (1.75 mM^{-1} s^{-1}) in comparison to that measured at 0.47 T.

Also, it is noteworthy that the mesoporous silica shell has been widely used in developing various kinds of bionanocomposites. Prototypical examples are those mesoporous shells with the magnetic (T_2) or optical nanoparticle cores that carry drugs for cancer diagnosis and treatment;[28,34–42] the outer silica shell then isolates the cores and prevents the aggregation of nanoparticles in the physiological environment. In this study, the H-MnO@mSiO_2(Ir)@PEG seems to be a very promising T_1 contrast agent and versatile nanocomposite for bioimaging and drug delivery. Details of the relevant applications are elaborated upon as follows.

***In Vitro* Cellular Testing.** First of all, the toxicity of the nanoplatform is examined prior to the application in cells or tissue. In this study, the HeLa cell line, derived from the human cervical cancer cell, is chosen for cytotoxicity evaluation. The cells are cultured in 90% minimum essential medium (MEM; Cellgro Herndon, VA, USA) supplemented with 10% heat-inactivated fetal bovine serum, penicillin (50 U/mL), and streptomycin (0.05 mg/mL). For cell expansion and senescence induction, the cells are cultured at 37 °C in a humidified atmosphere of 5% CO_2/95% air and passaged by trypsinization. To examine the cytotoxicity, various concentrations of nanocomposites, 5, 10, 20, 40, 50, and 100 μg/mL, are added to each HeLa cell sample and incubated for 24 h. As for the H-MnO@mSiO_2(Ir)@PEG, the result of the MTT (3-(4,5-dimethylthiazol-2-yl)-2,5-diphenyltetrazolium bromide) test shown in Figure S9 of the Supporting Information reveals that almost 100% of the cells are viable even after incubation with a dose of as high as 100 μg/mL.

We then demonstrate a unique three-in-one property of the as-prepared H-MnO@mSiO_2(Ir)@PEG nanocomposite, namely, the luminescence imaging, magnetic resonance imaging, and PDT. The confocal microscopy images and fluorescence staining are first performed to ensure interaction between the as-prepared nanocomposite and HeLa cells. In this experiment, HeLa cells incubated with 100 μg/mL of H-MnO@mSiO_2(Ir)@PEG for 2 h are fixed with paraformaldehyde solution and stained with dyes 4′,6-diamidino-2-phenylindole (DAPI) and Alexa Fluor 488 phalloidin

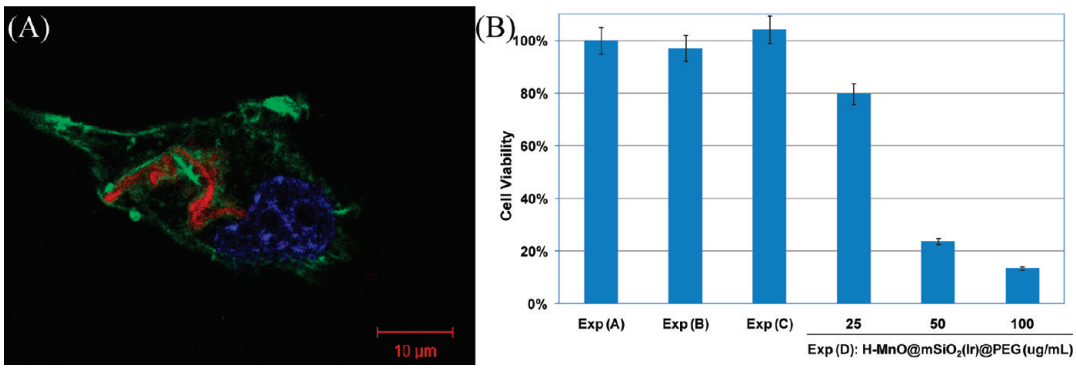

Figure 6. (A) Confocal image of HeLa cell treated with 100 μg/mL MnO@mSiO$_2$(Ir)@PEG. The nucleus, cytoskeleton, and the nanoparticles are shown in blue, green, and red, respectively. (B) After PDT test, the MTT assay was then performed under various experimental conditions: (1) EXP(A) cells with no nanoparticles and no light exposure; (2) EXP(B) cells with no nanoparticles but with light exposure (30 min, 200 mW); (3) EXP(C) cell with 100 μg/mL nanoparticles (incubated for 120 min) but without light exposure; (4) EXP(D) cells with a series of dose-dependent concentrations 25, 50, 100 μg/mL, and under light exposure.

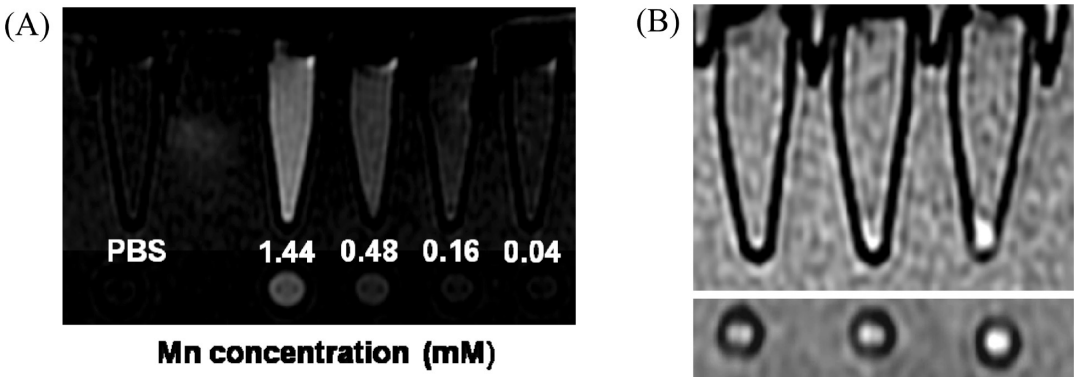

Figure 7. (A,B) Side and bottom view of MR imaging. (A) T_1-weighted images of H-MnO@mSiO$_2$(Ir)@PEG as a function of manganese oxide. (B) T_1-weighted images of different conditions. From left to right: PBS buffer, HeLa cells, HeLa cells treated with 100 μg/mL H-MnO@mSiO$_2$(Ir)@PEG.

for nucleus and cytoskeleton labeling, respectively. The confocal image shown in Figure 6A clearly indicates that H-MnO@mSiO$_2$(Ir)@PEG of red 600 nm phosphorescence was internalized into the cells and mainly resided in the cytoplasm close to the nuclei. Although the exact location of the particles was not fully determined, collective images from *Z*-stack scanning (see Figure S10 in Supporting Information) indicates that nearly none of particles are located on the cell membrane and inside the nucleus. Thus, the confocal imaging sufficiently illustrates efficient labeling and specific location characters of the H-MnO@mSiO$_2$(Ir)@PEG. To demonstrate the PDT capability, the HeLa cells are treated with H-MnO@mSiO$_2$(Ir)@PEG. The incubated cells with different concentrations of H-MnO@mSiO$_2$(Ir)@PEG particles before and after light exposure were then examined, and the results are summarized in Figure 6B. To ensure the apoptosis is solely caused by singlet oxygen, a variety of experiments have been performed, which are categorized as follows: (A) cells with no nanoparticles and no light exposure; (B) cells with no nanoparticles but with light exposure (30 min, 200 mW); (C) cells with 100 μg/mL nanoparticles (incubated for 120 min) but without light exposure; (D) cells with a series of dose-dependent concentrations from 25 to 100 μg/mL and under light exposure. As a result, we observed no sign of cell death in all controls (A), (B), and (C) under MTT assay, eliminating the possibility that cell death is caused by either nanocomposite toxicity or irradiation of the light source individually. In (D), as shown in Figure 6B, the viability of cells after simultaneous treatment of H-MnO@mSiO$_2$(Ir)@PEG and light drastically decreases (80 to 14%), which also reveals a dose-dependent relationship (25−100 μg/mL). The MR signals in T_1-weighted contrast imaging brightened as the concentration of Mn ions increased (see Figure 7A). The added concentration is further confirmed with inductively coupled plasma mass spectrometry (ICP-MS). Figure 7B shows the MR images of the collected cell pellets with or without H-MnO@mSiO$_2$(Ir)@PEG treatment. A significant signal intensity change in the MRI study is clearly indicative of H-MnO@mSiO$_2$(Ir)@PEG labeling capability and could be used for cell tracing. The combination of these results demonstrates a promising biocompatible H-MnO@mSiO$_2$(Ir)@PEG

nanocomposite in phosphorescence imaging, MRI, and photodynamic therapy.

CONCLUSION

In summary, several remarks can be pointed out in this study. First, using EA/NaOH(aq), a new and facile method to prepare uniform hollow MnO NPs has been demonstrated. In-depth investigation of the etching mechanism indicates that the acetate anion plays a key role, which acts as a ligand to chelate the metal (Mn) ion and then extrude the core MnO *via* Kirkendall effect, forming hollow MnO (H-MnO) nanoparticles. To optimize the biocompatibility of H-MnO NPs, we further synthesized the H-MnO@mSiO$_2$ NPs, in which the mesoporous silica possesses three distinct topological domains that can be independently functionalized: (1) the silica framework, (2) the worm-like nanochannels, and (3) the nanocomposite's outermost surface. A systematic investigation of the r_1 relaxivity property was then carried out among various types of MnO nanocomposites, and the results show promising r_1 relaxivity for H-MnO@mSiO$_2$ NPs. To achieve multifunctionality, a highly emissive Ir(III) complex, which serves as both photosensitizer and the luminescent chromophore, is incorporated into the silica framework *via* the sol−gel chemistry. The worm-like nanochannels not only enhance PDT efficacy by enabling the free diffusion of oxygen but also increase water permeability to interior hollow manganese oxide core, enhancing the T_1 signal. Finally, the PEG, a biocompatible polymer, is then anchored on the outermost surface to maintain the pore structure. Also, its nonfouling property avoids protein adsorption and then bypasses the RES system in *in vivo* applications. Thus, the results presented herein provide a facile and novel approach for developing trifunctional T_1 MRI contrast agents combining optical imaging and photodynamic therapy inside a mesoporous silica nanoparticle.

METHODS

Chemicals. 1-Octadecene (technical grade, 90%, Acros), oleic acid (90%, Acros), manganese chloride tetrahydrate ($MnCl_2 \times 4H_2O$, 99%, Aldrich), hexanol (98%, Acros), Triton X-100 (Acros), tetraethyl orthosilicate (98%, Acros), ammonium hydroxide (28−30 wt %, Fluka), 2-[methoxy(polyethyleneoxy)propyl]trimethoxysilane (PEG_{500}-silane, M_w = 460−590, tech-90, Gelest), and ammonium nitrate (≥99.0%, Aldrich), cetyltrimethylammonium bromide (CTAB, 99%, Acros), sodium carbonate (Na_2CO_3, Showa), triethoxysilane ($HSi(OEt)_3$, Alfa Aesar), platinum divinyltetramethyldisiloxane (Pt(dvs), Aldrich), sodium hydroxide, ethyl acetate, hexane, isopropyl alcohol, and chloroform were used without further purification.

Ir(III) Complex Sensitizer. The highly emissive, alkene-functionalized Ir(III) complex [Ir(piq)$_2$(pp-butylene)] was prepared by treatment of [(piq)$_2$Ir(μ-Cl)]$_2$ with the pyridyl pyrazole (pp-butylene)H and Na_2CO_3 in refluxing 2-methoxyethanol. The $(EtO)_3$Si-functionalized Ir(III) complex [Ir(piq)$_2$(ppTES)] was subsequently prepared using [Ir(piq)$_2$(pp-butylene)], triethoxysilane, and Pt(dvs) in toluene. After stirring at reflux for 15 h, the solvent was evaporated under vacuum and the unreacted silane reagent was removed by repeated hexane washes. Spectral data of [Ir(piq)$_2$(pp-butylene)]: MS (FAB, ^{193}Ir) m/z = 798 (M^+); ^{1}H NMR (400 MHz, acetone-d) δ = 9.06−9.00 (m, 2H), 8.3 (dd, 2H, J_{HH} = 13.2, 12 Hz), 7.96−8.02 (m, 2H), 7.72−7.84 (m, 7H), 7.6 (d, 1H, J_{HH} = 6.8 Hz), 7.53 (d, 1H, J_{HH} = 6.4 Hz), 7.42−7.46 (m, 2H), 7.02 (t, 1H, J_{HH} = 16.8 Hz), 6.90−6.97 (m, 2H), 6.82 (t, 1H, J_{HH} = 14.8 Hz), 6.65 (t, 1H, J_{HH} = 30 Hz), 6.55 (s, 1H), 6.52 (d, 1H, J_{HH} = 8.4 Hz), 6.36 (d, 1H, J_{HH} = 7.6 Hz), 5.76−5.86 (m, 1H), 4.94 (d, 1H, J_{HH} = 22.4 Hz), 4.83 (d, 1H, J_{HH} = 12.4 Hz), 2.54−2.61 (m, 2H), 2.24−2.3 (m, 2H). Spectral data of [Ir(piq)$_2$(ppTES)]: MS(FAB, ^{193}Ir) m/z = 962 (M^+); ^{1}H NMR (400 MHz, $CDCl_3$) δ = 8.97−8.89 (m, 2H), 8.23 (dd, 2H, J_{HH} =14.2, 8.0 Hz), 7.81−7.75 (m, 2H), 7.68−7.57 (m, 7H), 7.52 (d, 1H, J_{HH} = 6.0 Hz), 7.48 (d, 1H, J_{HH} = 5.6 Hz), 7.25 (d, 1H, J_{HH} = 4.8 Hz), 7.14 (d, 1H, J_{HH} = 6.8 Hz), 7.01 (q, 2H, J_{HH} = 5.6 Hz), 6.85−6.78 (m, 3H), 6.46 (d, 1H, J_{HH} = 7.6 Hz), 6.45 (s, 1H), 6.39 (d, 1H, J_{HH} = 7.2 Hz), 3.67−3.79 (m, 6H; OCH_2Me), 2.59−2.66 (m, 2H), 1.54−1.64 (m, 2H), 1.15−1.31 (m, 11H), 0.56−0.63 ppm (m, 2H).

MnO Nanocrystals. Manganese oxide nanocrystals (NCs) were prepared by the method described previously with some modifications.[21] Manganese oleate complex is prepared by the reaction of $MnCl_2 \cdot 4H_2O$ and oleic acid in methanol under basic conditions. Typically, 1.24 g of the manganese oleate is used and dissolved in 10 g of 1-octadecene. The mixture solution was degassed at 80 °C in order to remove any moisture and oxygen. The reaction mixture was subsequently treated with a definitive temperature program. First of all, the solution was rapidly heated to 200 °C at a rate of 5 °C/min. The solution was then further heated to 300 °C at a heating rate of 1.2 °C/min with vigorous stirring and maintained at the temperature for 1 h before cooling to room temperature. Solid samples were collected *via* centrifuging at 9000 rpm for 3 min, washing, and then redispersing the precipitate with hexane and isopropyl alcohol several times. Finally, the purified MnO nanocrystals are dispersed in 10 mL of hexane.

H-MnO Nanocrystals by Etching Process. Prior to the etching process, phase transfer of MnO nanocrystals dispersed in hexane was preceded as follows: First, dried manganese oxide NCs were dissolved in chloroform. Two milliliters of the NC solution (10−20 mg/mL) was mixed with 100 mg of cetyltrimethylammonium bromide (CTAB) and 20 mL of water. The mixture was then stirred vigorously, and the formation of the oil-in-water microemulsion appeared with a turbid brown solution. Then the chloroform solvent was boiled off from the solution, resulting in a transparent black MnO/CTAB solution. The solution was filtered through a 0.44 μm syringe filter to remove any large aggregates or contaminants. The etching process was performed by adding 0.5 mL of 0.4 M NaOH solution and 3 mL of ethylacetate to a mixture of 29.5 mL of water and MnO/CTAB solution. The mixture was heated to 60 °C and stirred for 10 h. Resulting H-MnO NPs were retrieved by repeating the procedures of centrifugation and then washing by repetition of dispersion in distilled water several times.

MnO@SiO$_2$ Nanoparticles. MnO nanocrystals with amorphous silica modification were prepared from reverse micelles by using a modified procedure we reported previously.[22]

MnO@mSiO$_2$(Ir)@PEG and H-MnO@mSiO$_2$(Ir)@PEG Nanoparticles. For coating mesoporous silica shells onto MnO nanocrystals, another 200 mg of CTAB, 0.5 mL of 0.4 M NaOH solution, 3 mL of ethanol, and 0.5 mL of tetraethylorthosilicate (TEOS) were added to a mixture of 29.5 mL of water and MnO/CTAB solution in sequence. The mixture was heated to 60 °C under stirring. After 30 min, 2 mg of Ir(III) complex was added and the solution was stirred for another 6 h. The as-synthesized materials were centrifuged and washed with ethanol. As for the formation of the hollow MnO core (H-MnO@mSiO$_2$(Ir)), the etching process mentioned previously was applied. Prior to the extraction of

surfactants (CTAB) from the NPs, surface modification of poly(ethylene glycol) (PEG) proceeded as follows: 2-[methoxy(polyethyleneoxy)propyl]trimethoxysilane (30 μL) was added to a mixture of ethanol (30 mL), DI water (6 mL), NH_4OH (300 μL), and the as-prepared nanoparticles (20 mg). After 24 h of stirring, the samples were centrifuged several times to remove the unreacted chemicals. To avoid the MnO dissolution that occurs under acidic conditions, the surfactants were removed *via* a fast and efficient ion exchange method where the as-synthesized MnO@mSiO_2(Ir)@PEG (H-MnO@mSiO_2(Ir)@PEG) NPs are transferred to 50 mL of ethanol containing 0.3 g of NH_4NO_3 and kept at 60 °C for 2 h. The extraction step was repeated twice to remove the surfactants. After 72 h of dialysis, the final product, MnO@mSiO_2(Ir)@PEG (H-MnO@mSiO_2(Ir)@PEG), was prepared and ready for use.

Confocal Fluorescence Imaging. For confocal microscopic observation, the HeLa cell were seeded in a 6-well plate with 5×10^4 cell/well density in 2 mL of serum-free culture medium to promote the uptake of nanoparticles. After 2 h incubation time with 100 μg/mL MnO@mSiO_2(Ir)@PEG, cells were washed three times with PBS and then fixed with 4% paraformaldehyde in PBS. The cells were washed twice with PBS and then incubated in 0.1% Triton X-100 for 5 min. In order to study confocal fluorescence imaging, 4′,6-diamidino-2-phenylindole (DAPI, Molecular Probes) and Alexa Fluor 488 phalloidin (Invitrogen) were chosen to stain the nucleus and cytoskeleton, respectively. The cells were stained with 5 μg/mL Alexa Fluor 488 phalloidin in 3% BSA for 30 min and 10 μg/mL DAPI for 5 min. The cells were washed twice with PBS and observed by a Zeiss LSM710 NLO confocal spectral microscope equipped with 63X (P-APO, 1.40 oil immersion) objective, and using 405 nm diode laser, 488 nm argon laser, and 543 nm He−Ne laser as excitation source.

***In Vitro* Cytotoxicity.** The cell viability was analyzed by using a colorimetric assay agent, 3-(4,5-dimethylthiazol-2-yl)-2,5-diphenyltetrazolium bromide (MTT, Roche). The HaLa cells were seeded in a 24-well plate with 5×10^4 cell per well in 90% minimum essential medium (MEM; Cellgro Herndon, VA, USA) supplemented with 10% heat-inactivated fetal bovine serum, penicillin (50 U/mL), and streptomycin (0.05 mg/mL). To contrast with control, six different dosages were added to each well: 5, 10, 20, 40, 50, and 100 μg/mL. After 24 h of incubation, wells were washed twice with PBS and then incubated with 500 μL of culture medium with 10% MTT (3-(4,5-dimethylthiazol-2-yl)-2,5-diphenyltetrazolium bromide) agent. After 3 h of reaction time, culture medium was removed and replenished with 300 μL of dimethyl sulfoxide (Sigma-Aldrich) to dissolve the purple MTT-formazan crystal. The absorbance was measured at 595 nm with fluorescence (VersaMax Microplate Spectrophotometers; Molecular-Devices). All of the conditions were done three times.

PDT toward HeLa Cells. The celluar effect of H-MnO@mSiO_2(Ir)@PEG was analyzed by PDT for cytotoxic effect. To promote the uptake of nanoparticles, the HeLa cells were seeded in a 24-well plate with 5×10^4 cell/well density in serum-free culture medium. To observe the dose-dependent relationship, four different dosages were added to the cell sample: 0, 25, 50, and 100 μg/mL. After 2 h incubation time, the cells were washed twice with PBS and replenished with culture medium. Each sample was treated under a fiber optic halogen light source at 200 mW for 30 min, which can eliminate the possible celluar damage caused by heat. The power of the light source was measured by a power meter. The treated cells were incubated with 500 μL of culture medium with 10% MTT (3-(4,5-dimethylthiazol-2-yl)-2,5-diphenyltetrazolium bromide) agent after being washed twice with PBS. After 3 h reaction time, culture medium was removed and replenished with 300 μL of dimethyl sulfoxide (Sigma-Aldrich). The absorbance was measured at 595 nm with fluorescence (VersaMax Microplate Spectrophotometers; Molecular-Devices). All of the conditions were done three times.

Relaxivity Measurement. Measurements of r_1 and r_2 relaxation times were made at 40 °C using a 0.47 T Minispec spectrometer (Bruker Minispec mq series relaxometer); r_2 relaxation times were determined using a Carr−Purcell−Meiboom−Gill (CPMG) sequence, recycle time 10 s, eight averages with phase cycling, and 180° pulse separation of 1 ms. Monoexponential fitting was performed to even echoes over 250 ms acquisition window. The r_1 relaxation was estimated using inversion recovery techniques, recycle time 10 s, four averages with phase cycling, and eight inversion times logarithmically spaced over the interval 0−2000 ms. Linear regression between r_1 and r_2 and manganese concentration was performed using standard techniques.

MRI Cell Sample Measurement. MRI was performed using a clinical 3 T MR system (Signa Infinite Twinspeed, GE Healthcare, USA). The cell samples were centrifuged in test tubes bathing in a homemade water tank. The tank was then placed in an 8 channel head coil. Two dimension T_2-weighted fast spin echo pulse sequences were used (TR/TE = 550/13 ms). The slice thickness was 1.5 mm with a 0.2 mm gap and the field of view (FOV) was 14 × 7 cm. The matrix size is 288 × 192. Total scan time was 2 min and 46 s at the NEX of 3. The images were then analyzed at the workstation provided by GE Healthcare (Advantage workstation 4.2).

Instrument Information. The as-prepared nanoparticles were characterized with a transmission electron microscope (Hitachi H-7100, 80 kV), powder X-ray diffractometer (model PANalytical X'Pert PRO), and high-resolution transmission electron microscope (JEOL JEM-2100F, 200 kV) including a CCD camera with Diffpack program. X-ray photoelectron spectrometry (XPS/ESCA) was done with a PHI 5000 VersaProbe scanning ESCA microprobe (ULVAC-PHI, Japan) using a microfocused, monochromatic Al Kα X-ray (25 W, 100 μm). Excitation and emission spectra were both recorded on an Edinburgh (FS920) fluorimeter. Hydrodynamic radii and surface charges were measured with a Zetasizer (Malvern Zetasizer 3000 HS).

Acknowledgment. This work is supported by the National Science Council, Taiwan. We thank Mr. Wei Chen for N_2 adsorption−desorption isotherm measurement.

Supporting Information Available: TEM image of MnO NCs dispersed in water, Kirkendall intermediates, size-controlled H-MnO@mSiO_2(Ir)@PEG, and MnO@SiO_2 nanoparticles, histogram analysis of H-MnO@mSiO_2(Ir)@PEG, excitation and emission spectra, DLS data and zeta-potential data of H-MnO@mSiO_2(Ir)@PEG nanoparticles, MTT assay results and CLSM *Z*-stack scanning images. This material is available free of charge *via* the Internet at http://pubs.acs.org.

REFERENCES AND NOTES

1. Caravan, P. Strategies for Increasing the Sensitivity of Gadolinium Based MRI Contrast Agents. *Chem. Soc. Rev.* **2006**, *35*, 512–523.
2. Sitharaman, B.; Kissell, K. R.; Hartman, K. B.; Tran, L. A.; Baikalov, A.; Rusakova, I.; Sun, Y.; Khant, H.; Ludtke, S. J.; Chiu, W.; *et al.* Superparamagnetic Gadonanotubes Are High-Performance MRI Contrast Agents. *Chem. Commun.* **2005**, 3915–3917.
3. Caravan, P.; Ellison, J. J.; McMurry, T. J.; Lauffer, R. B. Gadolinium(III) Chelates as MRI Contrast Agents: Structure, Dynamics, and Applications. *Chem. Rev.* **1999**, *99*, 2293–2352.
4. Zhang, C. F.; Jugold, M.; Woenne, E. C.; Lammers, T.; Morgenstern, B.; Mueller, M. M.; Zentgraf, H.; Bock, M.; Eisenhut, M.; Semmler, W.; *et al.* Specific Targeting of Tumor Angiogenesis by RGD-Conjugated Ultrasmall Superparamagnetic Iron Oxide Particles Using a Clinical 1.5-T Magnetic Resonance Scanner. *Cancer Res.* **2007**, *67*, 1555–1562.
5. Martina, M. S.; Fortin, J. P.; Menager, C.; Clement, O.; Barratt, G.; Grabielle-Madelmont, C.; Gazeau, F.; Cabuil, V.; Lesieur, S. Generation of Superparamagnetic Liposomes Revealed as Highly Efficient MRI Contrast Agents for *In Vivo* Imaging. *J. Am. Chem. Soc.* **2005**, *127*, 10676–10685.
6. Kircher, M. F.; Mahmood, U.; King, R. S.; Weissleder, R.; Josephson, L. A Multimodal Nanoparticle for Preoperative Magnetic Resonance Imaging and Intraoperative Optical Brain Tumor Delineation. *Cancer Res.* **2003**, *63*, 8122–8125.

7. Lai, C. W.; Wang, Y. H.; Uttam, B. P.; Chen, Y. C.; Hsiao, J. K.; Liu, C. L.; Liu, H. M.; Chen, C. Y. One-Pot Solvothermal Synthesis of FePt/Fe_3O_4 Core–Shell Nanoparticles. *Chem. Commun.* **2008**, 5342–5344.
8. Merbach, A. E.; Toth, E. *The Chemistry of Contrast Agents in Medical Magnetic Resonance Imaging*; John Wiley & Sons: New York, 2001.
9. Na, H. B.; An, K.; Park, Y. I.; Park, M.; Lee, I. S.; Nam, D. H.; Kim, S. T.; Kim, S. H.; Kim, S. W.; Lim, K. H.; *et al.* Development of a T_1 Contrast Agent for Magnetic Resonance Imaging Using MnO Nanoparticles. *Angew. Chem., Int. Ed.* **2007**, *46*, 5397–5401.
10. Shin, J.; Anisur, R. M.; Ko, M. K.; Im, G. H.; Lee, J. H.; Lee, I. S. Hollow Manganese Oxide Nanoparticles as Multifunctional Agents for Magnetic Resonance Imaging and Drug Delivery. *Angew. Chem., Int. Ed.* **2009**, *48*, 321–324.
11. Schladt, T. D.; Schneider, K.; Shukoor, M. I.; Natalio, F.; Bauer, H.; Tahir, M. N.; Weber, S.; Schreiber, L. M.; Schroder, H. C.; Muller, W. E. G.; *et al.* Highly Soluble Multifunctional MnO Nanoparticles for Simultaneous Optical and MRI Imaging and Cancer Treatment Using Photodynamic Therapy. *J. Mater. Chem.* **2010**, *20*, 8297–8304.
12. Lai, C. W.; Wang, Y. H.; Chen, Y. C.; Hsieh, C. C.; Uttam, B. P.; Hsiao, J. K.; Hsua, C. C.; Chou, P. T. Homogenous, Far-Reaching Tuning and Highly Emissive QD–Silica Core–Shell Nanocomposite Synthesized *via* a Delay Photoactive Procedure: Their Applications in Two-Photon Imaging of Human Mesenchymal Stem Cells. *J. Mater. Chem.* **2009**, *19*, 8314–8319.
13. Yang, H.; Zhuang, Y.; Hu, H.; Du, X.; Zhang, C.; Shi, X.; Wu, H.; Yang, S. Silica-Coated Manganese Oxide Nanoparticles as a Platform for Targeted Magnetic Resonance and Fluorescence Imaging of Cancer Cells. *Adv. Funct. Mater.* **2010**, *20*, 1–9.
14. An, K.; Kwon, S. G.; Park, M.; Na, H. B.; Baik, S. I.; Yu, J. H.; Kim, D.; Son, J. S.; Kim, Y. W.; Song, I. C.; *et al.* Synthesis of Uniform Hollow Oxide Nanoparticles through Nanoscale Acid Etching. *Nano Lett.* **2008**, *8*, 4252–4258.
15. Yi, D. K.; Selvan, S. T.; Lee, S. S.; Papaefthymiou, G. C.; Kundaliya, D.; Ying, J. Y. Silica-Coated Nanocomposites of Magnetic Nanoparticles and Quantum Dots. *J. Am. Chem. Soc.* **2005**, *127*, 4990–4991.
16. Lee, D. C.; Mikulec, F. V.; Pelaez, J. M.; Koo, B.; Korgel, B. A. Synthesis and Magnetic Properties of Silica-Coated FePt Nanocrystals. *J. Phys. Chem. B* **2006**, *110*, 11160–11166.
17. Selvan, S. T.; Patra, P. K.; Ang, C. Y.; Ying, J. Y. Synthesis of Silica-Coated Semiconductor and Magnetic Quantum Dots and Their Use in the Imaging of Live Cells. *Angew. Chem., Int. Ed.* **2007**, *46*, 2448–2452.
18. Tan, H.; Xue, J. M.; Shuter, B.; Li, X.; Wang, J. Synthesis of PEOlated Fe_3O_4@SiO_2 Nanoparticles *via* Bioinspired Silification for Magnetic Resonance Imaging. *Adv. Funct. Mater.* **2010**, *20*, 722–731.
19. Chen, F. H.; Zhang, L. M.; Chen, Q. T.; Zhang, Y.; Zhang, Z. J. Synthesis of a Novel Magnetic Drug Delivery System Composed of Doxorubicin-Conjugated Fe_3O_4 Nanoparticle Cores and a PEG-Functionalized Porous Silica Shell. *Chem. Commun.* **2010**, *46*, 8633–8635.
20. Dai, Q.; Lam, M.; Swanson, S.; Yu, R. H. R.; Milliron, D. J.; Topuria, T.; Jubert, P. O.; Nelson, A. Monodisperse Cobalt Ferrite Nanomagnets with Uniform Silica Coatings. *Langmuir* **2010**, *26*, 17546–17551.
21. Schladt, T. D.; Graf, T.; Tremel, W. Synthesis and Characterization of Monodisperse Manganese Oxide Nanoparticles—Evaluation of the Nucleation and Growth Mechanism. *Chem. Mater.* **2009**, *21*, 3183–3190.
22. Lai, C. W.; Wang, Y. H.; Lai, C. H.; Yang, M. J.; Chen, C. Y.; Chou, P. T.; Chan, C. S.; Chi, Y.; Chen, Y. C.; Hsiao, J. K. Iridium-Complex-Functionalized Fe_3O_4/SiO_2 Core/Shell Nanoparticles: A Facile Three-in-One System in Magnetic Resonance Imaging, Luminescence Imaging, and Photodynamic Therapy. *Small* **2008**, *4*, 218–224.
23. Nooney, R. I.; Thirunavukkarasu, D.; Chen, Y.; Josephs, R.; Ostafin, A. E. Self-Assembly of Mesoporous Nanoscale Silica/Gold Composites. *Langmuir* **2003**, *19*, 7628–7637.
24. Lin, Y. S.; Haynes, C. L. Synthesis and Characterization of Biocompatible and Size-Tunable Multifunctional Porous Silica Nanoparticles. *Chem. Mater.* **2009**, *21*, 3979–3986.
25. Everett, D. H. Definitions, Terminology and Symbols in Colloid and Surface Chemistry. *Pure Appl. Chem.* **1972**, *31*, 577–638.
26. Lin, Y. S.; Haynes, C. L. Impacts of Mesoporous Silica Nanoparticle Size, Pore Ordering, and Pore Integrity on Hemolytic Activity. *J. Am. Chem. Soc.* **2010**, *132*, 4834–4842.
27. Lewinski, N.; Colvin, V.; Drezek, R. Cytotoxicity of Nanoparticles. *Small* **2008**, *4*, 26–49.
28. Gorelikov, I.; Matsuura, N. Single-Step Coating of Mesoporous Silica on Cetyltrimethyl Ammonium Bromide-Capped Nanoparticles. *Nano Lett.* **2008**, *8*, 4252–4258.
29. Taylor, K. M. L.; Rieter, W. J.; Lin, W. Manganese-Based Nanoscale Metal–Organic Frameworks for Magnetic Resonance Imaging. *J. Am. Chem. Soc.* **2008**, *130*, 14358–14359.
30. Na, H. B.; Hyeon, T. Nanostructured T_1 MRI Contrast Agents. *J. Mater. Chem.* **2009**, *19*, 6267–6273.
31. Huang, C. C.; Khu, N. H.; Yeh, C. S. The Characteristics of Sub 10 nm Manganese Oxide T_1 Contrast Agents of Different Nanostructured Morphologies. *Biomaterials* **2010**, *31*, 4073–4078.
32. Huang, J.; Xie, J.; Chen, K.; Bu, L.; Lee, S.; Cheng, Z.; Li, X.; Chen, X. HSA Coated MnO Nanoparticles with Prominent MRI Contrast for Tumor Imaging. *Chem. Commun.* **2010**, *46*, 6684–6686.
33. Baek, M. J.; Park, J. Y.; Xu, W.; Kattel, K.; Kim, H. G.; Lee, E. J.; Patel, A. K.; Lee, J. J.; Chang, Y.; Kim, T. J.; *et al.* Water-Soluble MnO Nanocolloid for a Molecular T_1 MR Imaging: A Facile One-Pot Synthesis, *In Vivo* T_1 MR Images, and Account for Relaxivities. *ACS Appl. Mater. Interfaces* **2010**, *2*, 2949–2955.
34. Kim, J.; Lee, J. E.; Lee, J.; Yu, J. H.; Kim, B. C.; An, K.; Hwang, Y.; Shin, C. H.; Park, J. G.; Kim, J.; *et al.* Magnetic Fluorescent Delivery Vehicle Using Uniform Mesoporous Silica Spheres Embedded with Monodisperse Magnetic and Semiconductor Nanocrystals. *J. Am. Chem. Soc.* **2006**, *128*, 688–689.
35. Kim, J.; Kim, H. S.; Lee, N.; Kim, T.; Kim, H.; Yu, T.; Song, I. C.; Moon, W. K.; Hyeon, T. Multifunctional Uniform Nanoparticles Composed of a Magnetite Nanocrystal Core and a Mesoporous Silica Shell for Magnetic Resonance and Fluorescence Imaging and for Drug Delivery. *Angew. Chem., Int. Ed.* **2008**, *47*, 8438–8441.
36. Liong, M.; Lu, J.; Kovochich, M.; Xia, T.; Ruehm, S. G.; Nel, A. E.; Tamanoi, F.; Zink, J. I. Multifunctional Inorganic Nanoparticles for Imaging, Targeting, and Drug Delivery. *ACS Nano* **2008**, *2*, 889–896.
37. Joo, S. H.; Park, J. Y.; Tsung, C. K.; Yamada, Y.; Yang, P.; Somorjai, G. A. Thermally Stable Pt/Mesoporous Silica Core–Shell Nanocatalysts for High-Temperature Reactions. *Nat. Mater.* **2009**, *8*, 126–131.
38. Lee, J. E.; Lee, N.; Kim, H.; Kim, J.; Choi, S. H.; Kim, J. H.; Kim, T.; Song, I. C.; Park, S. P.; Moon, W. K.; *et al.* Uniform Mesoporous Dye-Doped Silica Nanoparticles Decorated with Multiple Magnetite Nanocrystals for Simultaneous Enhanced Magnetic Resonance Imaging, Fluorescence Imaging, and Drug Delivery. *J. Am. Chem. Soc.* **2010**, *132*, 552–557.
39. Chen, Y.; Chen, H.; Guo, L.; He, Q.; Chen, F.; Zhou, J.; Feng, J.; Shi, J. Hollow/Rattle-Type Mesoporous Nanostructures by a Structural Difference-Based Selective Etching Strategy. *ACS Nano* **2010**, *4*, 529–539.
40. Chen, Y.; Chen, H.; Zeng, D.; Tian, Y.; Chen, F.; Feng, J.; Shi, J. Core/Shell Structured Hollow Mesoporous Nanocapsules: A Potential Platform for Simultaneous Cell Imaging and Anticancer Drug Delivery. *ACS Nano* **2010**, *4*, 6001–6013.
41. Feng, J.; Song, S. Y.; Deng, R. P.; Fan, W. Q.; Zhang, H. J. Novel Multifunctional Nanocomposites: Magnetic Mesoporous Silica Nanospheres Covalently Bonded with Near-Infrared Luminescent Lanthanide Complexes. *Langmuir* **2010**, *26*, 3596–3600.
42. Liu, J.; Qiao, S. Z.; Hu, Q. H.; Lu, G. Q. Magnetic Nanocomposites with Mesoporous Structures: Synthesis and Applications. *Small* **2011**, *7*, 425–443.